J Mater Sci (2014) 49:8031–8039
DOI 10.1007/s10853-014-8510-y

Fabrication of graphene-encapsulated $CoO/CoFe_2O_4$ composites derived from layered double hydroxides and their application as anode materials for lithium-ion batteries

Dejian Du · Wenbo Yue · Yu Ren · Xiaojing Yang

Received: 7 June 2014 / Accepted: 24 July 2014 / Published online: 3 August 2014

Abstract Bicomponent $CoO/CoFe_2O_4$ composites with tunable particle sizes are prepared using Co–Fe layered double hydroxides (LDHs) or Co–Fe hydroxides as precursors. Moreover, graphene-encapsulated $CoO/CoFe_2O_4$ composites (labeled as G-$CoO/CoFe_2O_4$) are fabricated by co-assembly of graphene oxide nanosheets and Co–Fe LDHs/hydroxides, and then thermal decomposition of Co–Fe LDHs/hydroxides. Compared to uncoated $CoO/CoFe_2O_4$, G-$CoO/CoFe_2O_4$ composites exhibit enhanced cycle performances and rate capabilities. The superior performance may be attributed to the graphene encapsulation that prevents the aggregation of $CoO/CoFe_2O_4$ particles, buffers the strain from the volume variation of $CoO/CoFe_2O_4$, and improves the electronic conductivity of the composite electrode. The electrochemical properties of G-$CoO/CoFe_2O_4$ can be further improved by reducing the particle size of $CoO/CoFe_2O_4$ due to the enlarged interface between graphene nanosheets and $CoO/CoFe_2O_4$ particles.

Electronic supplementary material The online version of this article (doi:10.1007/s10853-014-8510-y) contains supplementary material, which is available to authorized users.

D. Du · W. Yue (✉) · X. Yang (✉)
Beijing Key Laboratory of Energy Conversion and Storage Materials, College of Chemistry, Beijing Normal University, Beijing 100875, People's Republic of China
e-mail: wbyue@bnu.edu.cn

X. Yang
e-mail: yang.xiaojing@bnu.edu.cn

Y. Ren
National Institute of Clean-and-low-carbon Energy, Beijing 102209, People's Republic of China

Introduction

Rechargeable lithium-ion batteries (LIBs) are one of the most popular types of battery for portable electronics (e.g., laptops) due to many advantages such as high energy density, long cycle life, no memory effect, and environmental friendliness [1, 2]. As promising anode materials for LIBs, metal oxides and their hybridization have been widely investigated because of their high theoretical capacities and relative abundance [3–5]. However, some drawbacks limit their practical applications, including particle aggregation, severe volume change of metal oxides during cycles, and poor electronic conductivity, which eventually lead to capacity fading upon cycling [6, 7]. Recently, to overcome the issue of inferior cycling stability and rate capacity for metal oxide anodes in LIBs, bicomponent metal oxides composites, such as $Co_3O_4@MnO_2$ composites, have been prepared and show better electrochemical properties than each component of the composites due to their superior synergistic effect in electrochemical reaction [8, 9]. Notwithstanding, much effort has been still devoted to fabricate an smart integrated architecture using a simple and facile approach, in which the interface/chemical distributions of bicomponent metal oxides composites are homogeneous at the nanoscale.

LDHs, also known as anionic or hydrotalcite-like clays, are described by a general formula of $\left[M^{2+}_{1-x}M^{3+}_{x}(OH)_2\right]^{x+}\left[A^{n-}_{x/n}\right]^{x-}\cdot mH_2O$, where M^{2+}/M^{3+} is divalent/trivalent metal cation and A is n-valent interlayer guest anion [10, 11]. LDHs have triggered tremendous interest due to their wide applications as catalysts, luminescent materials, supercapacitor electrodes, and drug carriers [12–15]. In particular, they could also serve as precursors for the preparation of bicomponent metal oxide composites, which may be used as

high-performance anode materials for LIBs [16]. For instance, CoO/$CoFe_2O_4$ composites derived from Co–Fe LDHs exhibited good cycle performance and rate capability, which may be attributed to the homogenous dispersion of bicomponent active CoO and $CoFe_2O_4$ phases [17]. The CoO particles were separated efficiently and spatially by the coexisting $FeCo_2O_4$ phase, exhibiting a superior synergistic effect. However, the critical problems mentioned above for metal oxides still exist and need to be overcomed.

As a novel two-dimensional carbon matrix, graphene has attracted enormous attention due to its extraordinary properties such as high electrical conductivity, unusual mechanical strength, and ultralarge specific surface area [18]. Therefore, it is usually used as a matrix to support active materials for the improvement of their performances instead of normal carbon materials [19, 20]. For instance, graphene-based metal oxides and their hybridization exhibit superior electrochemical performances due to the graphene substrate that buffers the strain from the volume variation of metal oxides and enhances the electronic conductivity of graphene-based metal oxides [21–24]. In our previous work, we successfully prepared graphene-encapsulated mesoporous metal oxides by a modified stepwise heterocoagulation method [25, 26]. Herein, we describe a novel strategy for the preparation of G-CoO/$CoFe_2O_4$ composites derived from GO-encapsulated Co–Fe LDHs (labeled as GO-CoFe-LDHs), which showed better electrochemical performances than uncoated CoO/$CoFe_2O_4$ composites. GO-CoFe-LDHs were first synthesized by co-assembly of negatively charged GO nanosheets and positively charged layers of LDHs generated by the replacement of a portion of divalent metal cations with trivalent cations. Subsequently, G-CoO/$CoFe_2O_4$ composites were obtained after thermal treatment of GO-CoFe-LDHs under N_2 protection. Moreover, the CoO/$CoFe_2O_4$ and G-CoO/$CoFe_2O_4$ composites with large particle size (labeled as CoO/$CoFe_2O_4$-L and G-CoO/$CoFe_2O_4$-L) were also prepared by thermal decomposition of Co–Fe hydroxides and GO-encapsulated Co–Fe hydroxides (labeled as GO-CoFe-OHs), respectively. The effect of particle size of CoO/$CoFe_2O_4$ on their electrochemical properties was also investigated.

Experimental

Materials

The materials used in the experiment are as follows: cobalt nitrate hexahydrate ($Co(NO_3)_2{\cdot}6H_2O$, Sinopharm Chemical Reagent Co. Ltd, AR), iron nitrate nonahydrate ($Fe(NO_3)_3{\cdot}9H_2O$, Shantou Xilong Chemical Factory Guangdong, AR), cobalt chloride hexahydrate ($CoCl_2{\cdot}6H_2O$, Sinopharm Chemical Reagent Co. Ltd, AR), chloride tetrahydrate ($FeCl_2{\cdot}4H_2O$, Tianjin Bodi Chemical Co., AR), sodium hydroxide (NaOH, Beijing Chemical Works, AR), sodium carbonate (Na_2CO_3, Beijing Chemical Works, AR), and hexamethylenetetramine (HMT) ($C_6H_{12}N_4$, Shantou Xilong Chemical Factory Guangdong, AR).

Preparation of Co–Fe LDHs and Co–Fe hydroxides

Co–Fe LDHs with small particle size and Co–Fe hydroxides with large particle size were prepared according to the literature methods [10, 17]. In a typical synthesis of Co–Fe LDHs, 9.3 g of $Co(NO_3)_2{\cdot}6H_2O$ and 6.5 g of $Fe(NO_3)_3{\cdot}9H_2O$ was dissolved in 40 mL of distilled water. 3.1 g of NaOH and 3.4 g of Na_2CO_3 were dissolved in another 40 mL of distilled water. The two solutions were added simultaneously into a 250 mL beaker under vigorous stirring. The mixed solution was then transferred into a teflon-lined stainless steel autoclave and heated at 80 °C for 48 h. After cooling down to room temperature, the Co–Fe LDHs were collected by centrifugation, washed with water, and dried at 60 °C. In a typical synthesis of Co–Fe hydroxides, 0.95 g of $CoCl_2{\cdot}6H_2O$ and 0.40 g of $FeCl_2{\cdot}4H_2O$ were dissolved in 400 mL of distilled water. 6.3 g of HMT was dissolved in another 400 mL of distilled water. The two solutions were added simultaneously into a 1000 mL flask with vigorous stirring under N_2 protection. The mixed solution was then heated at a refluxing temperature (120 °C) under continuous stirring for 5 h. After cooling down to room temperature, the Co–Fe hydroxides were collected by centrifugation, washed with water, and dried at 60 °C.

Preparation of CoO/$CoFe_2O_4$ and G-CoO/$CoFe_2O_4$ composites

GO was synthesized from natural graphite powders by a modified Hummer's method (see the Supporting Information) [27]. G-CoO/$CoFe_2O_4$ composites were fabricated by co-assembly of graphene oxide nanosheets and Co–Fe LDHs, and then thermal decomposition of Co–Fe LDHs. In a typical process, 0.1 g of GO was dispersed in 80 mL of distilled water by ultrasonication for 1 h, and the pH of GO solution was then adjusted to $\sim$8.0 with aqueous ammonia. 0.15 g of Co–Fe LDHs (or hydroxides) was dispersed into another 80 mL of distilled water by ultrasonication for 0.5 h, and the suspension was added into the GO solution under mild magnetic stirring for 1 h. The resulting precipitate was collected by centrifugation, dried at 60 °C, and then placed into a tube furnace under N_2 protection for calcination. The temperature was increased from room temperature to 600 °C at a ramping rate of 2 °C min^{-1} and kept at that temperature for 2 h. The G-CoO/$CoFe_2O_4$ composites were obtained after being cooled down to the room temperature. For comparison, the CoO/$CoFe_2O_4$

composites were also prepared by thermal treatment of Co–Fe LDHs (or hydroxides) under the same condition.

Sample characterization

Specimens were initially characterized using X-ray diffraction (XRD) on a Phillips X'pert Pro MPD diffractometer with Cu K_α radiation. The zeta-potentials of the GO and Co–Fe LDHs suspensions were measured by a ZetaPlus zeta potential analyzer (Brookhaven Instruments Corporation). The Fourier transform infrared (FT-IR) spectra were recorded on a nicolet-380 fourier transform infrared spectrometer in the range of 400–4000 cm^{-1}. X-ray photoelectron (XPS) spectra were recorded on a Shimadzu Axis Ultra spectrometer with an Mg $K_\alpha = 1253.6$ eV excitation source. Further characterization was performed using transmission electron microscopy (TEM), high-resolution TEM (HRTEM) on a JEOL JEM-2011 electron microscope operated at 200 kV, and scanning electron microscope (SEM) on a JEOL JSM-6700F electron microscope at an accelerating voltage of 1 kV.

Electrochemical measurements

For electrochemical characterization, the composite electrodes were fabricated by mixing the active materials, acetylene black and polyvinylidene difluoride (PVDF) dissolved in N-methyl-2-pyrrolidine (NMP) in a weight ratio of 70:15:15. The mixed slurry was pressed onto a copper foil and dried at 110 °C in vacuum for 24 h. Cell assembly was carried out in an Ar-filled glove box. The electrolyte was 1 M solution of $LiPF_6$ dissolved in a EC:DEC:DMC solution with a 1:1:1 volume ratio. Electrochemical performances were measured using a CR2032-type coin cell with lithium metal as the negative electrode. The galvanostatic charge–discharge performance was measured with a LAND test system at the room temperature, and the voltage range was from 0.01 to 3.0 V (versus Li/Li^+), with a constant current of 100–1000 mA g^{-1}. Cyclic voltammetry tests were performed between 0.01 and 3.0 V with a scan rate of 0.5 mV s^{-1}, and the electrochemical impedance spectroscopy (EIS) was carried out in the frequency range from 100 kHz to 10 mHz on a Princeton PARSTAT 4000 electrochemical station.

Results and discussion

Morphology and structural characterization

Figure 1a shows the overall synthesis procedure of CoO/$CoFe_2O_4$ and G-CoO/$CoFe_2O_4$. GO nanosheets were first negatively charged in a weak alkaline solution (pH = ~8),

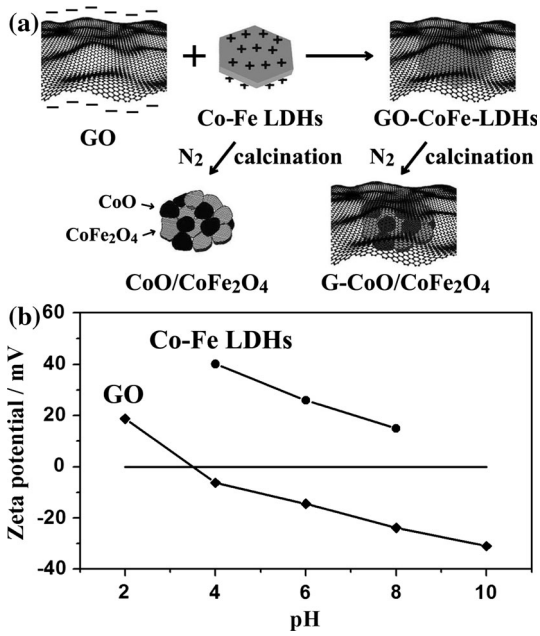

Fig. 1 **a** Schematic illustration of the synthesis route for CoO/$CoFe_2O_4$ and G-CoO/$CoFe_2O_4$ composites. **b** Zeta potentials of GO and Co–Fe LDHs in aqueous solution at different pH values

and then wrapped the positively charged Co–Fe LDHs through their electrostatic interaction. The zeta potentials of GO and Co–Fe LDHs in aqueous solution at different pH values are shown in Fig. 1b. Apparently, the surface of GO and Co–Fe LDHs was oppositely charged over the pH range of 4–8, and thus Co–Fe LDHs could be adsorbed onto GO nanosheets. Afterward, CoO/$CoFe_2O_4$ and G-CoO/$CoFe_2O_4$ composites were obtained by calcination of Co–Fe LDHs and GO-CoFe-LDHs in N_2 atmosphere, respectively.

The morphology and structure of Co–Fe LDHs/hydroxides and their decomposition products were elucidated by SEM and TEM. As shown in Fig. S1, both Co–Fe hydroxides and Co–Fe LDHs exhibited a characteristic platelet-like morphology. Moreover, the particle size of Co–Fe hydroxides was more than 1 μm in diameter, much larger than that of Co–Fe LDHs (200–250 nm in diameter). Their decomposition products (CoO/$CoFe_2O_4$) had similar morphologies, except for the formation of various pores in composites. The presence of pores may increase the interface between the electrolyte and the CoO/$CoFe_2O_4$ composite, and shorten the Li^+ ion diffusion length. Moreover, the particle size of CoO/$CoFe_2O_4$ can be simply controlled by the fabrication of different Co–Fe precursors, which is also related to the migration of Li^+ ions and the volume change of metal oxides. Figure 2a–d show the SEM and TEM images of GO-CoFe-LDHs and G-CoO/$CoFe_2O_4$, respectively. The transparent and wrinkled graphene/GO nanosheets could be observed and completely wrapped Co–Fe LDHs or CoO/$CoFe_2O_4$ composites. HRTEM image of G-CoO/$CoFe_2O_4$ (Fig. 2e)

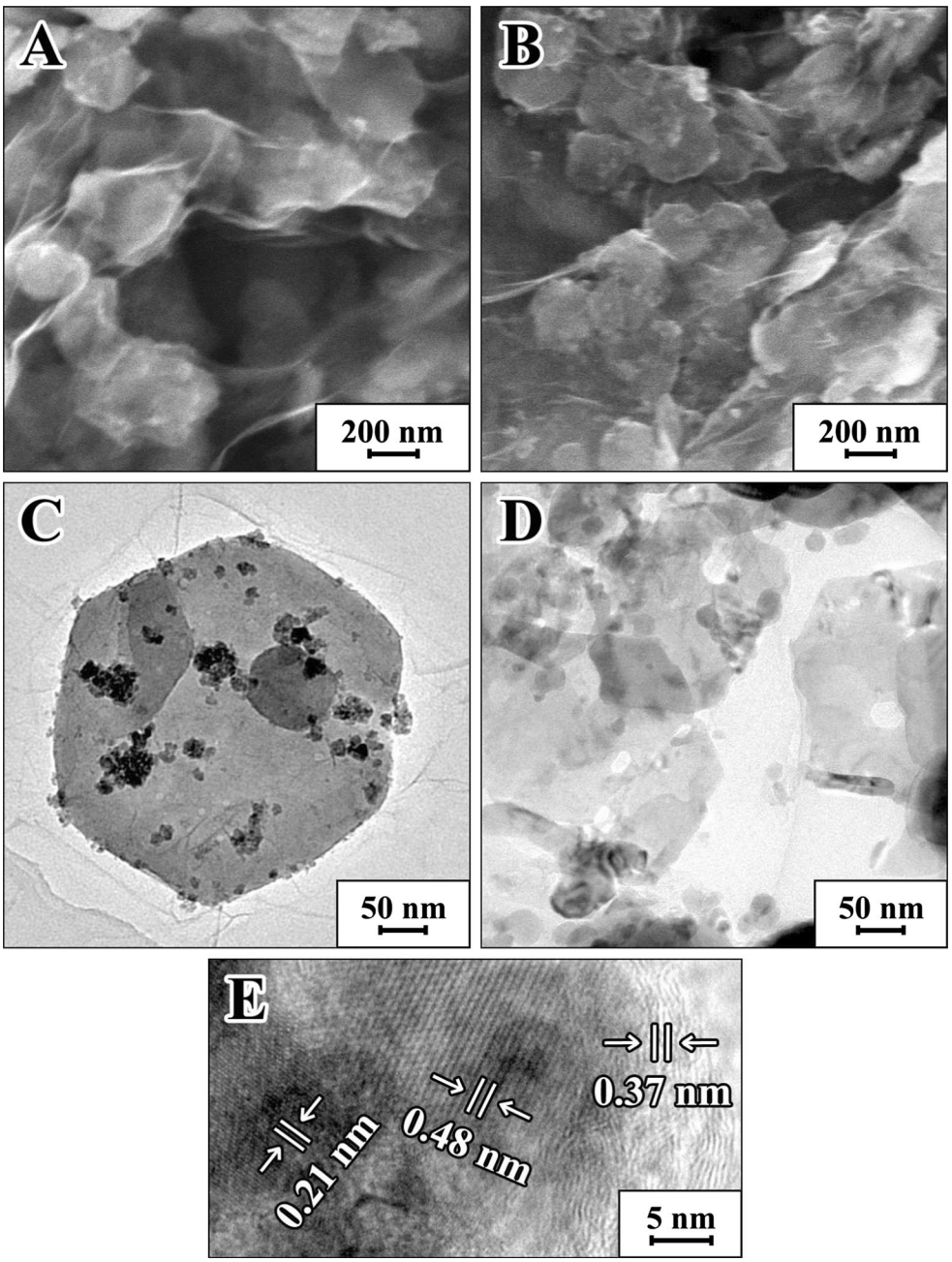

Fig. 2 SEM and TEM images of **a**, **c** GO-CoFe-LDHs, and **b**, **d** G-CoO/$CoFe_2O_4$. HRTEM image of **e** G-CoO/$CoFe_2O_4$

revealed that the nanoparticles exhibited a well-defined lattice spacing of ~0.21 and ~0.48 nm, corresponding to the (200) plane of CoO crystal and (111) plane of $CoFe_2O_4$ crystal, respectively. In addition, the CoO and $CoFe_2O_4$ crystals were separated with each other, and the synergistic effect of CoO/$CoFe_2O_4$ can be expected. 3–5 layer graphene nanosheets with a lattice spacing of ~0.37 nm were observed at the edge of G-CoO/$CoFe_2O_4$, corresponding to the basal spacing of highly reduced GO [28], but larger than that of graphite (~0.34 nm). It is interesting that Co–Fe hydroxides could be also wrapped by GO nanosheets using the same method based on the SEM and TEM observations (Fig. 3). The possible explanation is that Fe^{2+} in Co–Fe hydroxides was unstable and easily oxidized to Fe^{3+} by O_2 in air and GO in solution [10], which gave the layers of hydroxides positive charge.

The phase composition of specimens was further determined by XRD. The characteristic peaks in XRD patterns of Co–Fe LDHs and Co–Fe hydroxides (Fig. 4) could be indexed as a rhombohedral and a brucite-like

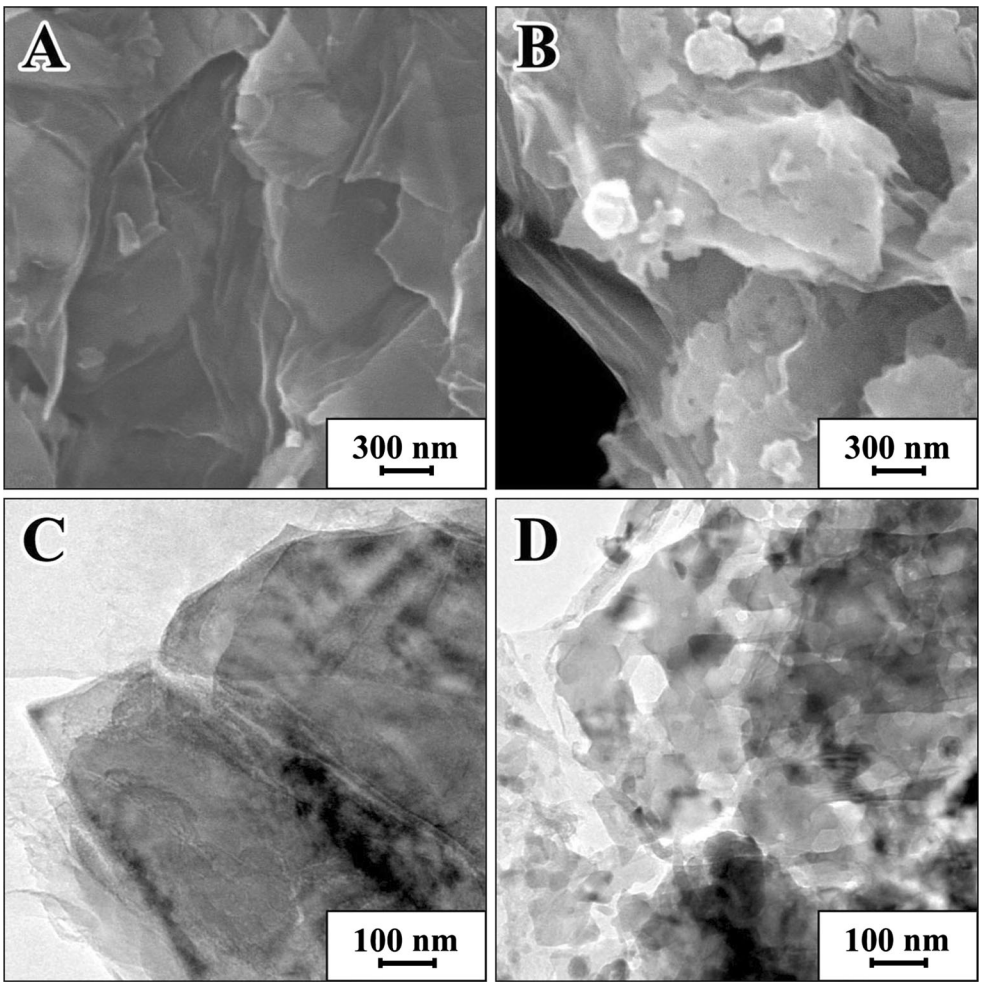

Fig. 3 SEM and TEM images of **a**, **c** GO-CoFe-OHs, and **b**, **d** G-CoO/$CoFe_2O_4$-L

structure, respectively, which were consistent with previous reports [10, 17]. The basal spacing of Co–Fe LDHs was expanded to ~0.76 nm due to the intercalated anions, in contrast with an initial value of ~0.46 nm for brucite-like Co–Fe hydroxides. The XRD results of their decomposition products showed the two-phase coexistence of CoO and $CoFe_2O_4$, implying the formation of G-CoO/$CoFe_2O_4$. The disappearance of GO peak at ~11° and graphene peak at ~26° indicated that the aggregation or restacking of GO/graphene nanosheets was prevented. The reduction degree of GO in G-CoO/$CoFe_2O_4$ was evaluated by FT-IR and XPS. Figure 5a shows the FT-IR spectra of GO and G-CoO/$CoFe_2O_4$. In the FT-IR spectrum of GO, the absorption bands at ca. 1728, 1383, 1223, 1063, and 1620 cm^{-1} were assigned to the stretching vibrations of C=O (carboxyl or carbonyl), O–H (carboxyl or intercalated water), C–OH (hydroxyl), C–O (epoxy or alkoxy), and the skeletal vibration of C=C from unoxidized graphitic domains, respectively. However, the C=O and C–O bands disappeared in the spectrum of G-CoO/$CoFe_2O_4$, and the intensity of the C=C band was higher than that of the C–OH band, demonstrating that most of the oxygen-containing groups of GO were eliminated [29]. Four elements (C, O, Fe, and Co) were detected in a survey XPS spectrum of G-CoO/$CoFe_2O_4$ (Fig. 5b), suggesting the presence of graphene and CoO/$CoFe_2O_4$ in the composite. Furthermore, the peaks corresponding to Co $2p_{3/2}$ and Co $2p_{1/2}$ doublet with binding energies of 780.0 and 795.5 eV, Fe $2p_{3/2}$ and Fe $2p_{1/2}$ doublet with binding energies of 711.5 and 724.9 eV could be observed in the Co 2p and Fe 2p XPS spectra of G-CoO/$CoFe_2O_4$ (Fig. 5c, d), respectively, which were characteristic of CoO/$CoFe_2O_4$ and agreed with the previous report [24]. The C 1s XPS spectra of GO and G-CoO/$CoFe_2O_4$ (Fig. 5e) showed four peaks at 284.6, 286.6, 287.6, and 288.8 eV, which could be assigned to the carbon atoms in different functional groups (C–C, C–O, C=O, and O=C–O) [29]. The relative content of C–O, C=O, and O=C–O bonds decreased sharply after hydrothermal treatment, indicating the high reduction degree of GO in G-CoO/$CoFe_2O_4$. The XPS characterization of

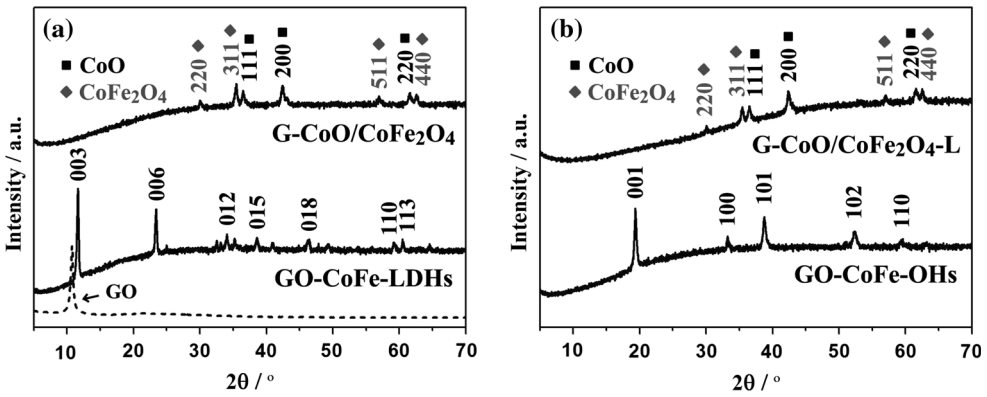

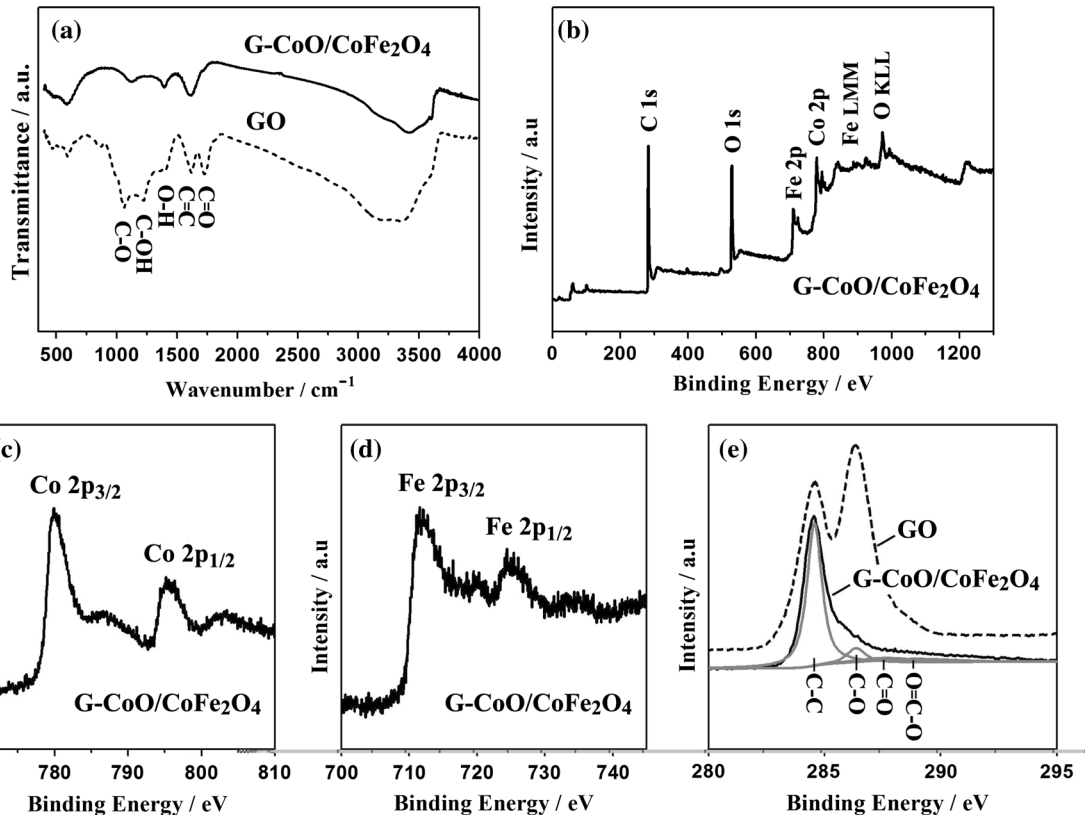

Fig. 4 XRD patterns of **a** GO, GO-CoFe-LDHs, G-CoO/$CoFe_2O_4$, and **b** GO-CoFe- OHs and G-CoO/$CoFe_2O_4$-L

Fig. 5 **a** FT-IR spectra of GO and G-CoO/$CoFe_2O_4$. **b** Survey, **c** Co 2p, and **d** Fe 2p XPS spectra of G-CoO/$CoFe_2O_4$. **e** C 1s XPS spectra of GO and G-CoO/$CoFe_2O_4$

GO-CoFe-OHs was also performed to investigate the possible reaction happened on the surface of Co–Fe hydroxides. In the Fe 2p XPS spectrum of GO-CoFe-OHs (Fig. S2a), the peaks corresponding to Fe $2p_{3/2}$ and Fe $2p_{1/2}$ doublet were located at 711.4, 724.8 eV, similar to the Fe 2p XPS peaks of G-CoO/$CoFe_2O_4$, suggesting that Fe^{2+} in the surface layers of Co–Fe hydroxides was oxidized to Fe^{3+} [30]. Furthermore, compared to the C 1s peaks in spectrum of GO, the intensities of these peaks related to the oxidized groups decreased in the spectrum of GO-CoFe-OHs (Fig. S2b), illustrating that GO was partially reduced in GO-CoFe-OHs. Consequently, Co–Fe hydroxides were first positively charged owing to the oxidation Fe^{2+} to Fe^{3+} in the surface layers, and then wrapped by the reduced GO nanosheets.

Electrochemical performance

The electrochemical properties of CoO/$CoFe_2O_4$ and G-CoO/$CoFe_2O_4$ electrodes were investigated by cyclic voltammetry and galvanostatic measurements. Figure S3 shows the cyclic voltammograms (CV) of CoO/$CoFe_2O_4$ and G-CoO/$CoFe_2O_4$ in the 1st, 2nd, 3rd, and 5th cycles. In the first cathodic scan, two reduction peaks were observed

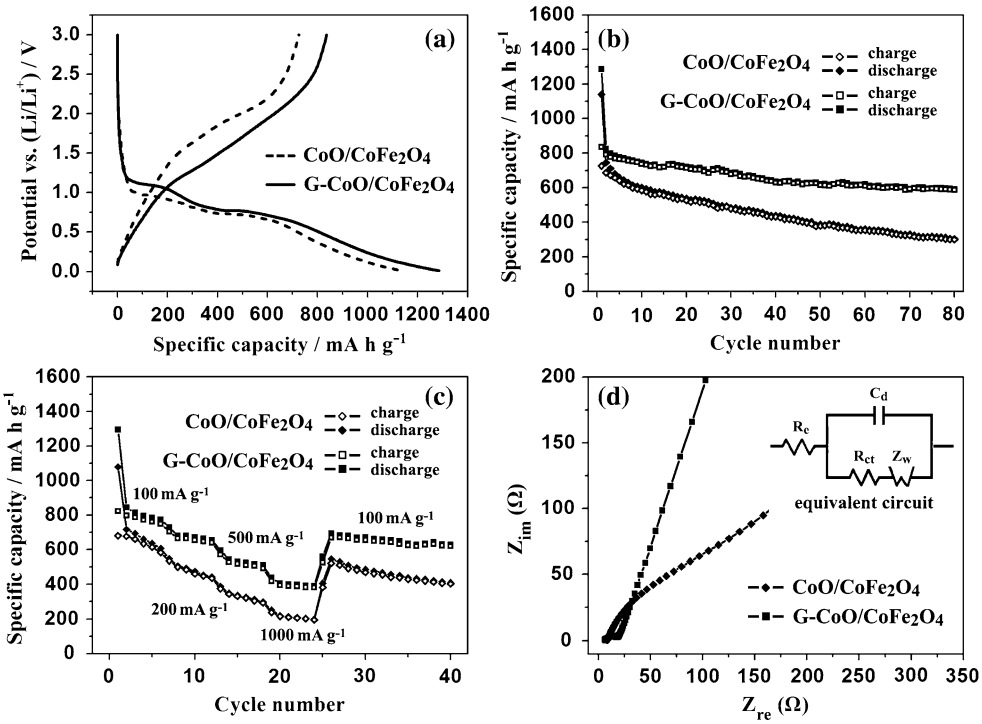

Fig. 6 **a** The first cycle charge–discharge curves for CoO/$CoFe_2O_4$ and G-CoO/$CoFe_2O_4$ at 100 mA g^{-1} in the voltage range 0.01–3.0 V. **b** Cycle performances of these samples at 100 mA g^{-1}. **c** Rate performances of these samples at 100–1000 mA g^{-1}. **d** The electrochemical impedance spectra of CoO/$CoFe_2O_4$ and G-CoO/$CoFe_2O_4$ after three cycles. The *inset* of **d** is the equivalent circuit model

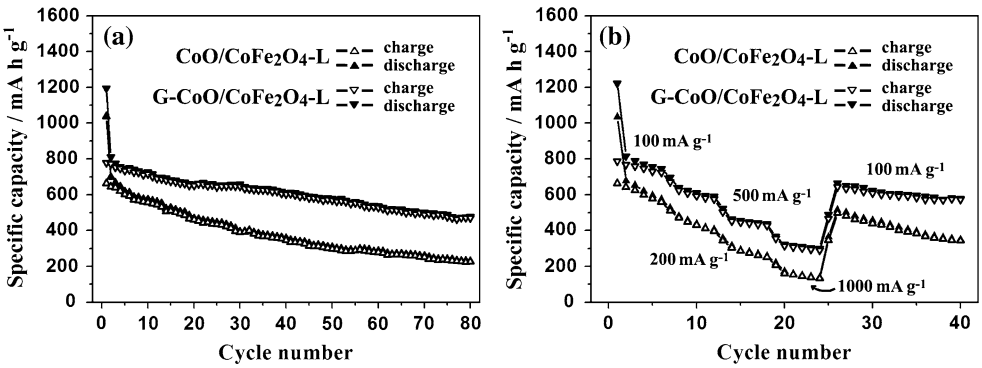

Fig. 7 **a** Cycle performances of CoO/$CoFe_2O_4$-L and G-CoO/$CoFe_2O_4$-L at 100 mA g^{-1}. **b** Rate performances of these samples at 100–1000 mA g^{-1}

at ~0.80 and ~0.41 V for CoO/$CoFe_2O_4$, ~1.10 and ~0.62 V for G-CoO/$CoFe_2O_4$, which could be assigned to the reduction of CoO–Co and $CoFe_2O_4$–Co&Fe, respectively [17]. In the first anodic scan, two overlapped oxidation peaks were present at ~2.12 and ~1.79 V for CoO/$CoFe_2O_4$, ~2.10 and ~1.77 V for G-CoO/$CoFe_2O_4$, corresponding to the oxidation of Co and Fe to CoO and Fe_2O_3, respectively [17]. The shift of reduction peak in the subsequent cycles might be related to the polarization of electrode. Furthermore, the almost overlapped CV curves of subsequent cycles (Fig. S3b) revealed a good cycleablity of G-CoO/$CoFe_2O_4$. Figure 6a shows the charge–discharge curves of CoO/$CoFe_2O_4$ and G-CoO/$CoFe_2O_4$ for the first cycle at 100 mA g^{-1}. There are two flat plateaus in the first-cycle discharge curve, which was in accordance with the CV results. The charge and discharge capacities of G-CoO/$CoFe_2O_4$ were ca. 836 and 1286 mA h g^{-1}, higher than those of CoO/$CoFe_2O_4$ (ca. 725 and 1139 mA h g^{-1}). The initial irreversible capacity loss could be mainly ascribed to the initial irreversible reaction and the formation of SEI layer. Figure 6b shows the cycle performances of CoO/$CoFe_2O_4$ and G-CoO/$CoFe_2O_4$ at 100 mA g^{-1}. After 80 cycles, the capacity of CoO/$CoFe_2O_4$ decreased dramatically to ~300 mA h g^{-1}, whereas a reversible capacity up to ~600 mA h g^{-1} was maintained for G-CoO/$CoFe_2O_4$. The rate capabilities of CoO/$CoFe_2O_4$ and G-CoO/$CoFe_2O_4$ at 100–1000 mA g^{-1} are shown in Fig. 6c. Apparently, G-CoO/$CoFe_2O_4$ also exhibited better rate capability than CoO/$CoFe_2O_4$. For instance, the capacity of G-CoO/$CoFe_2O_4$ at 1000 mA g^{-1} was ~400 mA h g^{-1}, much higher than that of CoO/$CoFe_2O_4$ (~220 mA h g^{-1}) at the same current density. Moreover,

the capacity of G-CoO/$CoFe_2O_4$ increased to ~630 mA h g^{-1} when the current density recovered to 100 mA g^{-1}, still higher than that of CoO/$CoFe_2O_4$ (~410 mA h g^{-1}). The superior electrochemical performance of G-CoO/$CoFe_2O_4$ may be ascribed to the graphene encapsulation, which separated CoO/$CoFe_2O_4$ composites, restrained the volume change of CoO/$CoFe_2O_4$, and enhanced the electrical conductivity of the composite electrode. The charge transport properties of these samples were characterized by EIS, and the equivalent circuit model is shown in the inset of Fig. 6d. The symbols of R_e, R_{ct}, C_d, and Z_w denoted the electrolyte resistance, the charge transfer resistance, the double layer capacitance, and the Warburg impedance, respectively [26]. Figure 6d shows the Nyquist plots containing a semicircle in the high frequency range and a sloping straight line in the low frequency range. Note that the radius of the semicircle for G-CoO/$CoFe_2O_4$ was much smaller than that for CoO/$CoFe_2O_4$, manifesting that the electrical conductivity of the electrode was improved by the introduction of graphene.

On the other hand, although the capacities of CoO/$CoFe_2O_4$ and G-CoO/$CoFe_2O_4$ electrodes decreased with enlarging the particle size of CoO/$CoFe_2O_4$, the cycle and rate performances of G-CoO/$CoFe_2O_4$-L were still better than those of CoO/$CoFe_2O_4$-L due to the graphene encapsulation (Fig. 7). For instance, the capacity of G-CoO/$CoFe_2O_4$-L was ~480 mA h g^{-1} at 100 mA g^{-1} after 80 cycles, larger than that of CoO/$CoFe_2O_4$-L (~230 mA h g^{-1}), and even larger than the theoretical capacity of graphite (~370 mA h g^{-1}). When the current density increased to 1000 mA g^{-1}, the capacity of G-CoO/$CoFe_2O_4$-L decreased to ~310 mA g^{-1}, but still larger than that of CoO/$CoFe_2O_4$-L (150 mA g^{-1}). The reduction of particle size of CoO/$CoFe_2O_4$ might be conducive to increase the electrode–electrolyte interface, shorten the diffusion paths of Li^+ ions and importantly, increase the interface between graphene nanosheets and CoO/$CoFe_2O_4$, giving rise to the improved electrochemical performances [26].

Conclusions

In this paper, we report a facile approach for the fabrication of G-CoO/$CoFe_2O_4$ as an anode material for LIBs. This novel composite was prepared by co-assembly of graphene oxide nanosheets and Co–Fe LDHs/hydroxides, and then thermal decomposition of Co–Fe LDHs/hydroxides. Compared to uncoated CoO/$CoFe_2O_4$, G-CoO/$CoFe_2O_4$ showed highly improved electrochemical properties such as higher reversible capacity and better cycle/rate performance. Moreover, the particle size of CoO/$CoFe_2O_4$ could be simply tuned by the control of the particle size of its precursors (Co–Fe LDHs or Co–Fe hydroxides), and highly influenced its electrochemical performance. This novel synthetic method may offer an attractive alternative approach for the preparation of graphene-encapsulated LDHs and their decomposition products with a wide range of applications.

Acknowledgements This work was financially supported by National Natural Science Foundation of China (21101014, 21273022 and 51272030).

References

1. Choi NS, Chen ZH, Freunberger SA, Ji XL, Sun YK, Amine K, Yushin G, Nazar LF, Cho J, Bruce PG (2012) Challenges facing lithium batteries and electrical double-layer capacitors. Angew Chem Int Ed 51:9994–10024
2. Su X, Wu QL, Li JC, Xiao XC, Lott A, Lu WQ, Sheldon BW, Wu J (2014) Silicon-based nanomaterials for lithium-ion batteries: a review. Adv Energy Mater 4:1300882
3. Wen ZG, Zheng F, Jiang ZR, Li MX, Luo YX (2013) Solvothermal synthesis of solid and hollow CoO nanospheres and their electrochemical properties in lithium-ion battery. J Mater Sci 48:342–347. doi:10.1007/s10853-012-6751-1
4. Yoon S, Bridges CA, Unocic RR, Paranthaman MP (2013) Mesoporous TiO_2 spheres with a nitridated conducting layer for lithium-ion batteries. J Mater Sci 48:5125–5131. doi:10.1007/s10853-012-7098-3
5. Yue WB, Jiang SH, Huang WJ, Gao ZQ, Li J, Ren Y, Zhao XH, Yang XJ (2013) Sandwich-structural graphene-based metal oxides as anode materials for lithium-ion batteries. J Mater Chem A 1:6928–6933
6. Yang S, Yue WB, Zhu J, Ren Y, Yang XJ (2013) Graphene-based mesoporous SnO_2 with enhanced electrochemical performance for lithium-ion batteries. Adv Funct Mater 23:3570–3576
7. Abbas SM, Hussain ST, Ali S, Ahmad N, Ali N, Abbas S (2013) Structure and electrochemical performance of ZnO/CNT composite as anode material for lithium-ion batteries. J Mater Sci 48:5429–5436. doi:10.1007/s10853-013-7336-3
8. Liu J, Jiang J, Cheng C, Li H, Zhang J, Gong H, Fan HJ (2011) Co_3O_4 nanowire@MnO_2 ultrathin nanosheet core/shell arrays: a new class of high-performance pseudocapacitive materials. Adv Mater 23:2076–2081
9. Meng TJ, Ara M, Wang LX, Naik R, Ng KYS (2014) Enhanced capacity for lithium-air batteries using $LaFe_{0.5}Mn_{0.5}O_3$–CeO_2 composite catalyst. J Mater Sci 49:4058–4066. doi:10.1007/s10853-014-8070-1
10. Ma RZ, Liu ZP, Takada K, Iyi N, Bando Y, Sasaki T (2007) Synthesis and exfoliation of Co^{2+}–Fe^{3+} layered double hydroxides: an innovative topochemical approach. J Am Chem Soc 129:5257–5263
11. Delorme F, Seron A, Vergnaud B, Galle-Cavalloni P, Jean-Prost V, Manguin J (2013) Evidence of the influence of the cationic composition on the anionic affinity of layered double hydroxides. J Mater Sci 48:5273–5279. doi:10.1007/s10853-013-7318-5
12. Wang Q, Tian SL, Long J, Ning P (2014) Use of Fe(II)Fe(III)-LDHs prepared by co-precipitation method in a heterogeneous-fenton process for degradation of methylene blue. Catal Today 224:41–48
13. Zhao YS, Li JG, Guo MX, Yang XJ (2013) Structural and photoluminescent investigation of LTbH/LEuH nanosheets and their color-tunable colloidal hybrids. J Mater Chem C 1:3584–3592

14. Huang S, Zhu GN, Zhang C, Tjiu WW, Xia YY, Liu TX (2012) Immobilization of Co–Al layered double hydroxides on graphene oxide nanosheets: growth mechanism and supercapacitor studies. ACS Appl Mater Interfaces 4:2242–2249
15. Yan L, Chen W, Zhu XY, Huang LB, Wang ZG, Zhu GY, Roy VAL, Yu KN, Chen XF (2013) Folic acid conjugated self-assembled layered double hydroxide nanoparticles for high-efficacy-targeted drug delivery. Chem Commun 49:10938–10940
16. Liu JP, Li YY, Huang XT, Li GY, Li ZK (2008) Layered double hydroxide nano-and microstructures grown directly on metal substrates and their calcined products for application as Li-ion battery electrodes. Adv Funct Mater 18:1448–1458
17. Li MX, Yin YX, Li CJ, Zhang FZ, Wan LJ, Xu SL, Evans DG (2012) Well-dispersed bi-component-active $CoO/CoFe_2O_4$ nanocomposites with tunable performances as anode materials for lithium-ion batteries. Chem Commun 48:410–412
18. Geim AK, Novoselov KS (2007) The rise of graphene. Nat Mater 6:183–191
19. Yue WB, Yang S, Ren Y, Yang XJ (2013) In situ growth of Sn, SnO on graphene nanosheets and their application as anode materials for lithium-ion batteries. Electrochim Acta 92:412–420
20. Yue WB, Tao SS, Fu JM, Gao ZQ, Ren Y (2013) Carbon-coated graphene-Cr_2O_3 composites with enhanced electrochemical performances for Li-ion batteries. Carbon 65:97–104
21. Guzman RC, Yang JH, Cheng MMC, Salley SO, Ng KYS (2013) A silicon nanoparticle/reduced graphene oxide composite anode with excellent nanoparticle dispersion to improve lithium ion battery performance. J Mater Sci 48:4823–4833. doi:10.1007/s10853-012-7094-7
22. Wu TH, Tu FY, Liu SQ, Zhuang SX, Jin GH, Pan CY (2014) MnO nanorods on graphene as an anode material for high capacity lithium ion batteries. J Mater Sci 49:1861–1867. doi:10.1007/s10853-013-7874-8
23. Guo R, Yue WB, An YM, Ren Y, Yan X (2014) Graphene-encapsulated porous carbon-ZnO composites as high-performance anode materials for Li-ion batteries. Electrochim Acta 135:161–167
24. Huo RJ, Jiang WJ, Xu SL, Zhang FZ, Hu JS (2014) Co/CoO/$CoFe_2O_4$/G nanocomposites derived from layered double hydroxides towards mass production of efficient Pt-free electrocatalysts for oxygen reduction reaction. Nanoscale 6:203–206
25. Jiang SH, Yue WB, Gao ZQ, Ren Y, Ma H, Zhao XH, Liu YL, Yang XJ (2013) Graphene-encapsulated mesoporous SnO_2 composites as high performance anodes for lithium-ion batteries. J Mater Sci 48:3870–3876. doi:10.1007/s10853-013-7189-9
26. Zhao L, Yue WB, Ren Y (2014) Synthesis of graphene-encapsulated mesoporous In_2O_3 with different particle size for high-performance lithium storage. Electrochim Acta 116:31–38
27. Hummers WS, Offeman RE (1958) Preparation of graphitic oxide. J Am Chem Soc 80:1339
28. Chen CF, Chen TT, Wang HL, Sun GB, Yang XJ (2011) A rapid, one-step, variable-valence metal ion assisted reduction method for graphene oxide. Nanotechnology 22:405602
29. Tao SS, Yue WB (2013) Controllable growth of metals on graphene nanosheets. RSC Adv 3:14299–14302
30. Tao SS, Yue WB, Zhong MY, Chen ZJ, Ren Y (2014) Fabrication of graphene-encapsulated porous carbon-metal oxide composites as anode materials for lithium-ion batteries. ACS Appl Mater Interfaces 6:6332–6339